



Article

Design of Hierarchical Nickel-Cobalt Phosphide/Nickel Oxide with Tunable Electronic Structure and Strong Chemical Interface for Advanced Supercapacitors

Gaini Zhang ^{1,2}, Jingqian Liu ^{1,2}, Hui Shan ^{3,*}, Zhengdong Ma ^{1,2}, Yuhui Xu ^{1,2}, Zihao Yang ^{1,2}, Jiaxuan Zuo ^{1,2}, Jingjing Wang ^{1,2}, Shufeng Li ^{4,*} and Xifei Li ^{1,2,*}

- ¹ Shaanxi International Joint Research Center of Surface Technology for Energy Storage Materials, Xi'an Key Laboratory of New Energy Materials and Devices, Institute of Advanced Electrochemical Energy & School of Materials Science and Engineering, Xi'an University of Technology, Xi'an 710048, China; zgn20051206@126.com (G.Z.); jinyl@xaut.edu.cn (J.L.); 1210113022@stu.xaut.edu.cn (Z.M.); 1230110017@stu.xaut.edu.cn (Y.X.); 1220110017@stu.xaut.edu.cn (Z.Y.); 1220110014@stu.xaut.edu.cn (J.Z.); wangjingjing@xaut.edu.cn (J.W.)
- ² Key Laboratory of Advanced Batteries Materials for Electric Vehicles of China Petroleum and Chemical Industry Federation, Xi'an University of Technology, Xi'an 710048, China
- ³ Key Laboratory of Magnetic Molecules and Magnetic Information Materials (Ministry of Education), School of Chemistry and Material Science, Shanxi Normal University, Taiyuan 030031, China
- ⁴ Xi'an Key Laboratory of Advanced Powder Metallurgy Materials and New Technology, Xi'an University of Technology, Xi'an 710048, China
- * Correspondence: shanhui@sxnu.edu.cn (H.S.); shufengli@xaut.edu.cn (S.L.); xfli@xaut.edu.cn (X.L.)



Citation: Zhang, G.; Liu, J.; Shan, H.; Ma, Z.; Xu, Y.; Yang, Z.; Zuo, J.; Wang, J.; Li, S.; Li, X. Design of Hierarchical Nickel-Cobalt Phosphide/Nickel Oxide with Tunable Electronic Structure and Strong Chemical Interface for Advanced Supercapacitors. *Batteries* **2023**, *9*, 584. <https://doi.org/10.3390/batteries9120584>

Academic Editors: Douglas Ivey and Seiji Kumagai

Received: 24 October 2023

Revised: 13 November 2023

Accepted: 27 November 2023

Published: 12 December 2023



Copyright: © 2023 by the authors. Licensee MDPI, Basel, Switzerland. This article is an open access article distributed under the terms and conditions of the Creative Commons Attribution (CC BY) license (<https://creativecommons.org/licenses/by/4.0/>).

Abstract: The design of a reasonable heterostructure electrode to achieve enhanced areal performance for supercapacitors remains a great challenge. Here, we constructed hierarchical porous NiCoP/NiO nanocomposites anchored on Ni foam with tunable electronic and structural properties, as well as robust interfacial interaction. In NiCoP/NiO, the interconnected NiO nanosheets serve as a carrier with enriched anchoring sites to confine the NiCoP and improve its stability. Meanwhile, the ultrathin NiCoP nanosheets with bimetallic centers are connected with porous NiO nanosheets to form a reliable heterojunction, enhancing the electrochemical reaction kinetics. Taking advantage of the synergistic contribution of bimetallic centers, phosphides and unique structure, the NiCoP/NiO delivers a high areal specific capacitance (1860 mF cm^{-2} at 5 mA cm^{-2}), good rate performance of 78.5% at six times the increased current density, and remarkable durability (11.0% decrease after 10,000 cycles). Furthermore, the assembled hybrid supercapacitor NiCoP/NiO//porous-activated carbon (PAC) delivers a high areal energy density of $173.7 \mu\text{Wh cm}^{-2}$ ($116.4 \mu\text{Wh cm}^{-2}$) at 1.6 mW cm^{-2} (32 mW cm^{-2}). The results indicate that the design of the heterostructure interface with strong chemical interface and tunable electronic structure is an effective and promising approach to boost the electrochemical performance for advanced supercapacitors.

Keywords: bimetallic phosphide; electronic structure; heterogeneous interface; rate capability; supercapacitor

1. Introduction

With the increase in energy use around the world, fossil fuels have caused serious environmental pollution and are becoming depleted. Therefore, on one hand, we must save existing energy, and on the other hand, we must develop new energy and efficient energy storage devices [1–3]. The current mainstream energy storage technology is electrochemical energy storage, which stores and releases electrical energy as chemical energy. Batteries and supercapacitors are mainly electrochemical energy storage devices. The former is known for storing more energy but releasing it more slowly. The latter integrates the characteristics of higher power output, rapid charge–discharge capability and long-term cyclic

lifespan [4–7]. Nonetheless, its relatively low energy density seriously hampers its practical application and development. Therefore, it is necessary to put more effort into developing electrochemical performance and boosting the energy density of supercapacitors [8,9]. As is well-known, capacitive materials have fast charging/discharging capability, while redox-active materials have excellent capacitive capability through quick and reversible Faradaic reactions, which in essence is similar to the battery-like redox reaction. Therefore, rational exploration of hybrid materials with well-defined microstructure/morphologies and optimized compositions would be an efficient approach to realize high electrochemical performance [10].

As potential redox-active pseudocapacitive electrode materials, transition metal oxides and hydroxides have high energy storage capacity based on Faradaic reactions and superior specific capacitances compared to typical carbon-based materials [11–13]. However, the low electrical conductivity of transition metal compounds, also including slow charge transfer rates and slow ion diffusion rates, result in drastically reduced capacitance at high current densities. In contrast, transition metal derivatives (sulfides [14–16], phosphides [17,18], selenides [19,20], etc.) have remarkable inherent electrical conductivity caused by a narrower bandgap. Therefore, transition metal phosphides (TMPs) have received extensive research attention for supercapacitors in virtue of their metalloid features, low band gaps and easy redox, which ensure the rapid electron transmission in active material and promote the redox reactions [21–23]. In particular, binary TMPs are a class of highly promising material due to their superior conductivity, adjustable compositions, and synergistic interaction between different metal ions [24,25], which consequently alter their electrochemical performance. Bimetallic nickel cobalt phosphides (NiCoP) stand out among the reported results for nickel-based and cobalt-based phosphides. NiCoP with different morphologies has been prepared via various synthetic processes. For instance, Hu et al. prepared Ni-Co phosphide nanoparticles with high conductivity and an adjustable Ni-Co proportion via a simple hydrothermal approach. It displays the prominent capacity of 571 C g^{-1} at 1 A g^{-1} [26]. Huang et al. reported the synthesis of ultrathin nickel cobalt phosphate electrodes using the electrodeposition strategy, and exhibited an outstanding specific capacity of 1768.5 C g^{-1} at 1 A g^{-1} [27]. Additionally, constructing a reasonable and simple architecture is considered to be a feasible approach to optimize the electrochemical property of TMPs. Wan et al. designed an optimum core-shell FeCoP@NiCoP composite via a facile two-step electrodeposition and subsequent phosphorization [28]. The NiCoP/Co₁Ni₂-MOF materials were synthesized by the anchoring of NiCoP nanoparticles onto Co₁Ni₂-MOF using a controllable partial phosphorization [29]. Although scientists have devoted great efforts in studying the composition and structure of nickel–cobalt phosphide, it is still a great challenge to design a reasonable heterostructured electrode to further improve the areal performance of supercapacitor.

Based on the above considerations, we report on a binder-free NiCoP/NiO electrode with 3D hierarchical porous structure growth on Ni foam (NF), prepared using oxidation–heat treatment and the electrodeposition method. Benefiting from the synergistic effect between unique structure and bimetallic center, the designed NiCoP/NiO electrode exhibited increased conductivity and surface capacitive contribution, and thus enhanced the areal specific capacitance, rate performance and long-term cycle stability, superior to NiO/NF and NiCoP/NF electrodes. Furthermore, a hybrid supercapacitor was assembled by applying the NiCoP/NiO as the positive electrode and porous activated carbon as the negative electrode. It affords high areal energy density and power density, and can illuminate the red light-emitting diode and digital timer for more than 25 min, showing its great application prospects in the field of energy storage, and also providing valuable insights for the development of high-performance electrodes for electrochemical energy storage systems.

2. Experimental Procedure

2.1. Fabrication of NiO Nanowall Arrays on Ni Foam

The well-trimmed Ni foam ($1\text{ cm} \times 2\text{ cm}$) was successively sonicated with 3.0 M HCl solution, acetone, ethanol and deionized water for 10 min to remove the surface impurities. Then, the treated NF was immersed into 20 mL of mixed solution containing NaOH (25 mM) and $(\text{NH}_4)_2\text{S}_2\text{O}_8$ (1.25 mM) for 6 h at the ambient temperature. Next, the NF was cleaned several times with deionized water and then vacuum-dried at 60°C . Finally, the electrode of porous NiO nanosheets arrays over NF substrate (denoted as NiO/NF) was obtained by annealing the obtained NF at 400°C for 2 h in a muffle furnace.

2.2. Synthesis of NiCoP/NiO Electrode

The NiCoP/NiO electrode was prepared by electrodepositing NiCoP onto NiO/NF in a three-electrode configuration, in which the NiO/NF, platinum foil ($1\text{ cm} \times 1\text{ cm}$) and Ag/AgCl were used as the working electrode, counter electrode and reference electrode, respectively. Typically, the deposition solutions were composed of 1.0 mM $\text{Co}(\text{NO}_3)_2 \cdot 6\text{H}_2\text{O}$, 1.0 mM $\text{NaH}_2\text{PO}_2 \cdot \text{H}_2\text{O}$, and 1.0 mM $\text{Ni}(\text{NO}_3)_2 \cdot 6\text{H}_2\text{O}$ in a 100 mL mixture of ethanol and water with a volume ratio of 1:1. The electrodynamic deposition was conducted at room temperature for 30 min while applying constant voltage of -1.0 V in 50 mL growth solution. After that, the resultant NiCoP/NiO electrode was rinsed and dried at 60°C under vacuum. Similarly, for comparison, the pure NiCoP/NF electrode was synthesized under the same conditions by using NF instead of NiO/NF as working electrode. Additionally, the NiCoP/NiO electrode with electrodeposition time of 15 min was also prepared.

2.3. Materials Characterization

X-ray diffraction (XRD) was performed using Shimadzu XRD-7000 instrument (Kyoto, Japan) to investigate the crystallographic phases of the materials. The architecture and morphology of the products were characterized by scanning electron microscopy (SEM) and transmission electron microscopy (TEM), which were carried out on FlexSEM 1000 (Hitachi High-Tech Corporation, Tokyo, Japan), Czech TESCAN MIRA LMS (Brno, Czech Republic) and JEOL JEM-F200 (Tokyo, Japan). The X-ray photoelectron spectroscopy (XPS) was performed using the K-Alpha (Thermo Scientific, Waltham, MA, USA), to identify the elemental compositions and valence states with a monochromatic Al $\text{K}\alpha$ source. The specific surface area of the samples was calculated using the Brunauer–Emmett–Teller (BET) method.

2.4. Electrochemical Measurement

Cyclic voltammetry (CV), galvanostatic charge–discharge (GCD) and electrochemical impedance spectroscopy (EIS) were evaluated on an electrochemical workstation (Jiangsu Donghua Analytical Instruments Co., Ltd., Jingjiang, China; DH7000) in a three-electrode configuration with 2.0 M KOH as electrolyte. Specifically, the prepared electrodes, platinum electrode ($1 \times 1\text{ cm}^2$) and Ag/AgCl electrode served as the working electrode, counter electrode and reference electrode, respectively. EIS operated from 0.01 Hz to 100 kHz via applying an alternating voltage of 10 mV amplitude. Hybrid supercapacitor was constructed using the prepared electrodes as the positive electrode, PAC as the negative electrode, and polypropylene membrane (Celgard 2400, Charlotte, NC, USA) as the separator. Negative electrode was prepared by casting a mixture of PAC, Super p and PVDF in N-methylpyrrolidone with the mass ratio of 8:1:1 on pre-cleaned NF ($1\text{ cm} \times 1\text{ cm}$) until both front and back surfaces were uniformly covered. Then, it was vacuum-dried at 60°C overnight before being pressed under 8.0 MPa.

Based on the GCD curves, the areal specific capacitance (C_a , mF cm^{-2}) was evaluated from the discharge curves using the following equation:

$$C_a = I\Delta t / (s\Delta V) \quad (1)$$

where I , Δt , s and ΔV represent the applied current (mA), discharge time (s), the geometric area of active electrode (cm^2), and the discharge potential window (V). The areal energy density (E_a , $\mu\text{Wh cm}^{-2}$) and power density (P_a , mW cm^{-2}) were calculated based on Equations (2) and (3), separately:

$$E_a = C_a \Delta V^2 / (2 \times 3.6) \quad (2)$$

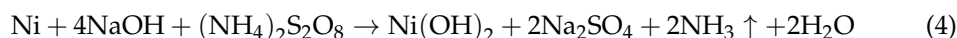
$$P_a = 3.6 E_a / \Delta t \quad (3)$$

where C_a , Δt and ΔV represent the areal specific capacitance (mF cm^{-2}), discharge time (s) and the cell voltage (V) of the whole device, respectively.

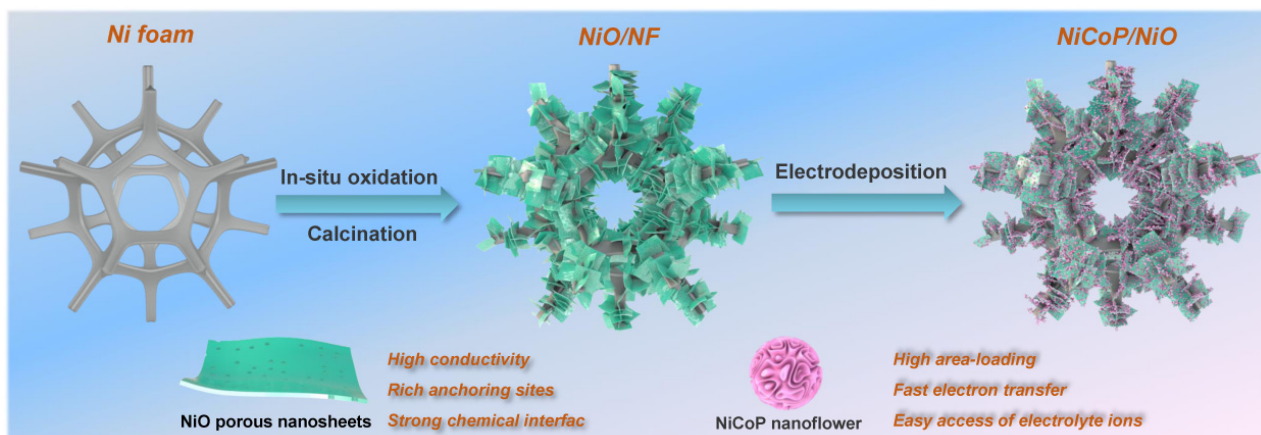
3. Results and Discussion

3.1. Morphology and Structure

The synthetic strategy for the hierarchical NiCoP/NiO nanocomposites supported on NF is schematically illustrated in Scheme 1. Initially, the Ni(OH)_2 nanowall arrays were anchored in situ on Ni foam via the partially oxidized Ni substrate in an alkaline-oxidized mixture solution of $(\text{NH}_4)_2\text{S}_2\text{O}_8$ and NaOH at room temperature. Subsequently, the porous NiO nanosheets arrays were obtained from the thermal decomposition of Ni(OH)_2 in a muffle furnace. Synthetic process of the NiO can be expressed in detail via the following formulas [30]:



The in situ grown NiO possesses remarkable mechanical adhesion on NF, which promotes good electrical contact and ensures efficient electrochemical reaction kinetics. Lastly, the porous NiO nanosheets were uniformly covered by the deposited NiCoP through a facile electrodeposition method. The three-dimensional interconnected NiO core not only serves as a backbone for the growth of NiCoP porous nanosheets but also facilitates the electronic transmission due to its high conductivity.



Scheme 1. Schematic illustration for synthesis process of hierarchical NiCoP/NiO composites on NF.

The morphology and microstructures of all the samples can be observed by SEM images. Pure NF has a 3D smooth skeleton and stable architecture without collapsing and cracking (Figure S1a,b), and can be used as a growth substrate for loading electroactive species. After immersing NF into an alkaline-oxidized solution and then calcining, the NiO nanowalls vertically anchor to the NF surface, and present a dense and ordered nanoarray structure (Figures 1a and S1c,d). It has a thickness of about 25 nm and the distance between two adjacent nanowalls is about 130 nm (Figure 1b). In addition, the interconnected network

consists of non-coalesced nanosheets and generates many macropores, which can offer highly convenient accesses for electrolyte diffusion and ensure the efficient utilization of active sites between electrolyte ions and electrode materials. Furthermore, growing active materials directly on the NF substrate can effectively avoid the generation of additional resistance caused by using binder and conductive materials. NiCoP was successfully decorated on the porous NiO nanowalls by electrodeposition. The generated NiCoP/NiO electrode exhibits interconnected mesh nanosheets, which uniformly adhere to the porous NiO nanowalls (Figure 1c,d). In some parts, the over-deposited NiCoP self-aggregates and forms flower-like structures. When the electrodeposition time is shortened, the 3D network structure similar to the NiO/NF substrate can be seen clearly (inset of Figure 1d), and the NiCoP is distributed homogeneously on the surface of NiO/NF nanowalls (Figure S2). This structure provides a larger number of electroactive sites and hierarchical channels, beneficial to highly effective availability of electrolyte ions and fast electron transport, and thus facilitating electrochemical energy storage. For comparison, the NiCoP was electrodeposited directly on the 3D NF framework under the same conditions. Figure 1e,f illustrate that the morphology changed slightly and formed a wrinkled plate-like structure, not at all flower-like. This may be concerned with the existence of grain boundaries over the NF surface. The resulting structure contains abundant macropores, indicating that the areal mass-loading of active materials is relatively low, which is not conducive to the formation of high areal-specific capacitance.

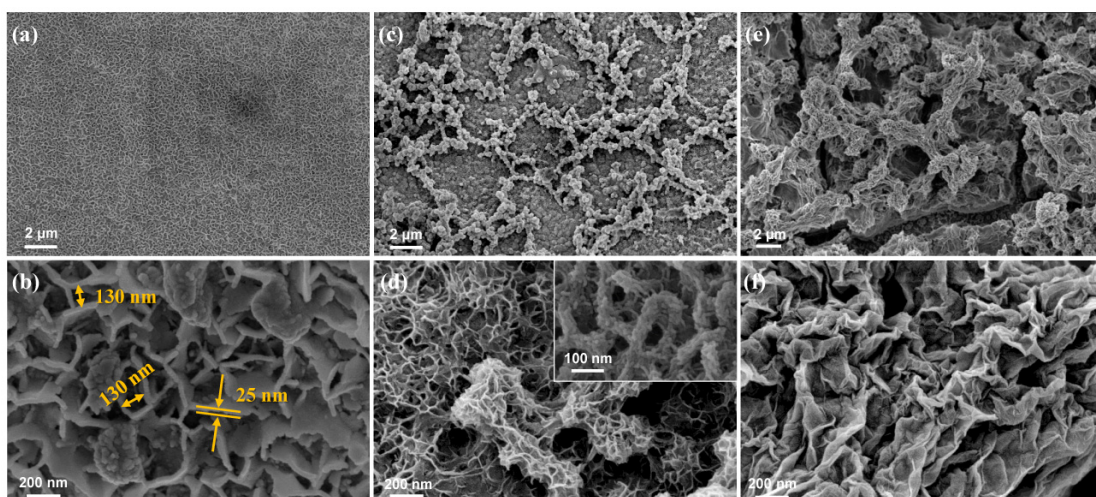


Figure 1. SEM images of (a,b) NiO/NF, (c,d) NiCoP/NiO and (e,f) NiCoP/NF.

In order to further analyze the detailed morphologies and microstructure information, the samples were removed from NF by the ultrasonic method for TEM and HRTEM characterizations. As for the NiO, the plate-like structure with numerous pores can be verified by the TEM image (Figure 2a). The formation of pores is mainly caused by the loss of water in the thermal decomposition process of $\text{Ni}(\text{OH})_2$. The lattice spacing of 0.146 nm is ascribed to the (220) lattice plane of NiO (Figure 2b). The NiCoP nanosheets have a large diameter-to-thickness ratio, and are highly transparent, suggesting their ultrathin structure (Figure 2c). They tightly adhere to the surface of the porous NiO nanowalls and form a hierarchical porous structure (Figure 2d,g). The special structure endows the NiO/NiCoP electrode with a large specific surface area ($132 \text{ m}^2 \cdot \text{g}^{-1}$) compared with NiO/NiCoP ($87 \text{ m}^2 \cdot \text{g}^{-1}$) (Figure S3), which is favorable for electrolyte permeation and ion diffusion, resulting in abundant active sites for electrochemical reactions. It indicates that the design of the core–shell structure is an effective strategy in increasing the areal-loading of active materials. HRTEM image shows the distinct heterointerface between NiCoP and NiO, as well as confirming the coexistence of both phases in the NiCoP/NiO. The clear lattice fringes with spacing of around 0.201 nm and 0.146 nm are consistent with the (201)

crystal planes of NiCoP (JCPDS No. 71-2336) and (220) planes of NiO, respectively (JCPDS No. 47-1049) (Figure 2e) [31,32]. Thanks to in situ nucleation growth coupled with good lattice matching, a close interfacial contact can be formed, which effectively facilitates the interfacial charge transfer and enhances ion diffusion kinetics during the electrochemical reaction process [32]. In addition, the selected-area electron diffraction (SAED) pattern exhibits well-defined diffraction rings, demonstrating the polycrystalline characteristics of the NiCoP/NiO composites (Figure 2f). In addition, the HAADF-STEM image (Figure 2h) and the corresponding elemental mapping results (Figure 2i) confirm the existence and homogeneous distribution of Ni, Co, P and O elements in the NiCoP/NiO, which further demonstrates the self-assembled NiCoP nanosheets are quite uniformly combined with porous NiO nanosheets.

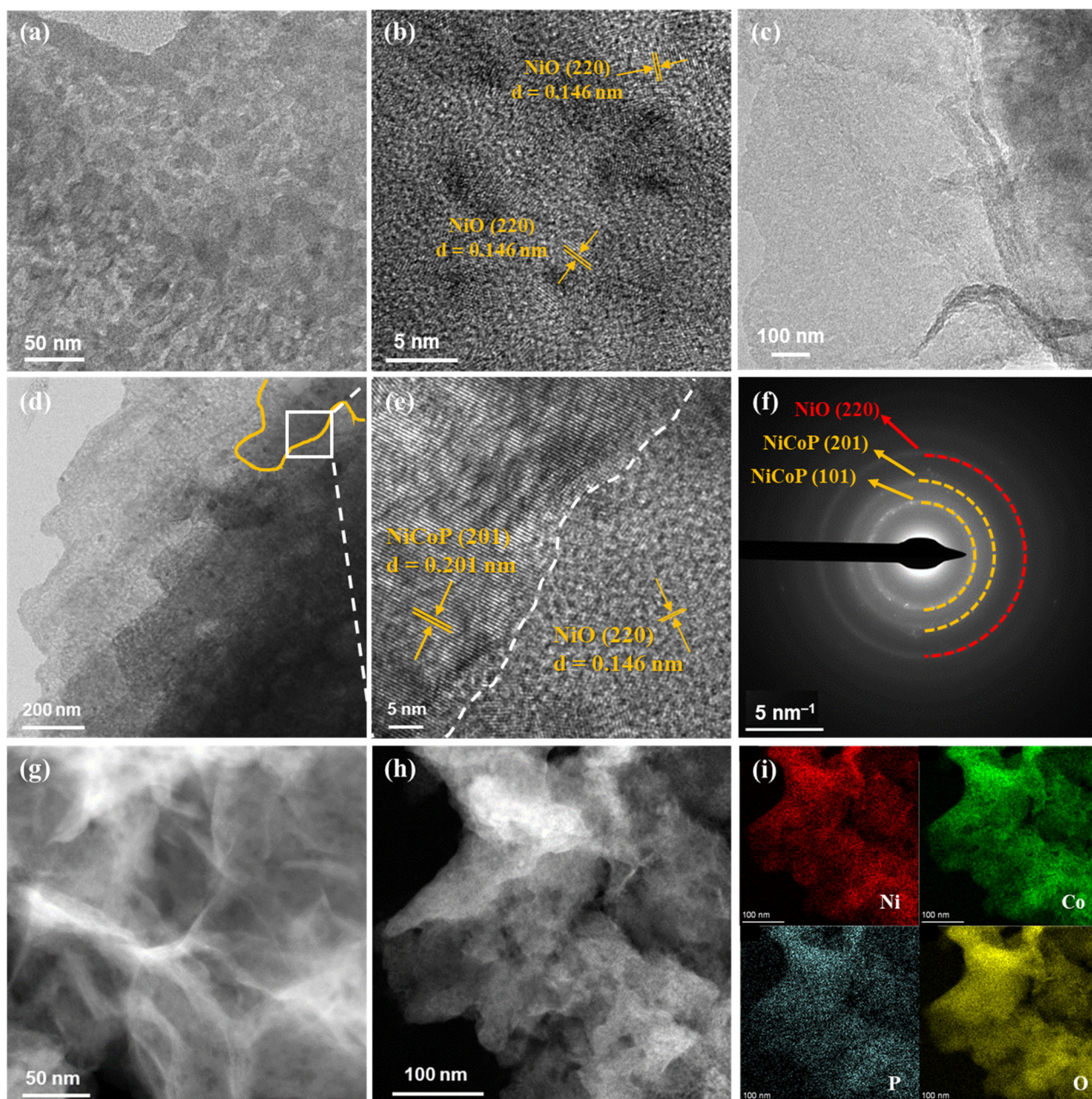


Figure 2. Morphology characterization of NiO, NiCoP and NiCoP/NiO composites: (a,b) TEM and HRTEM images of NiO; (c) TEM image of NiCoP; (d,e) TEM and HRTEM images of NiCoP/NiO; (f) corresponding SAED pattern; (g,h) HAADF-STEM images; and (i) EDS elemental mappings.

The XRD patterns of NiO/NF, NiCoP/NF and NiCoP/NiO are almost identical (Figure 3a). All the electrodes show three prominent diffraction peaks at 44.5°, 51.9° and 76.4°, which are in agreement with the crystal planes (111), (200) and (220) of the metal Ni (JCPDS No. 04-0850) [14]. Meanwhile, some weak diffraction peaks are observed in the XRD pattern of NiO/NF, which corresponds to NiO (JCPDS No. 47-1049). However, no extra diffraction peaks are observed in NiCoP/NF and NiCoP/NiO electrodes. Perhaps it is caused by the strong diffraction peak of NF, which covers the diffraction signal of NiCoP/NiO. Therefore, XPS analysis was performed to characterize the elemental composition and chemical valence, and further elucidate the synergistic effects of NiO and NiCoP. Compared with NiO/NF, XPS survey spectrum of NiCoP/NiO exhibits the signals of Co and P besides the Ni, O and C (Figure 3b), which matches well with the results of the EDS spectra. Among them, the C single may come from absorbed CO₂ [33,34]. Ni 2p spectra fitted by Gaussian fitting show two shakeup satellites and two distinctive spin-orbit doublets (Figure 3c). In NiCoP/NiO, the peaks at 856.2 and 873.5 eV are characteristic of Ni²⁺, while the peaks located at around 858.1 and 875.5 eV are ascribed to Ni³⁺ [35], accompanying two satellite peaks at 862.3 and 880.4 eV. The surface atomic ratios of Ni³⁺:Ni²⁺ in NiCoP/NF and NiCoP/NiO are 0.67:1 and 1.02:1 by calculating the peak areas, respectively. NiCoP/NiO obviously endows a higher oxidation state for Ni-sites than NiCoP/NF. The results suggest that the NiO substrate has a certain regulatory effect on the electronic structure of NiCoP. In addition, from the locally enlarged view of Figure 3c, another peak with lower binding energy is observed in NiCoP/NF and NiCoP/NiO electrodes are considered to be Ni^{δ+} species with a small positive charge ($0 < \delta < 2$) [36]. In addition to the characteristic peak of Ni²⁺, the peaks at around 853.4 and 870.9 eV can be observed in NiO/NF, which belong to the Metal Ni (Ni⁰) from nickel foam [37]. Figure 3d presents the Co 2p XPS spectroscopy for NiCoP/NF and NiCoP/NiO. In NiCoP/NiO, the Co 2p presents the photoelectron signals of Co²⁺, Co³⁺, and satellites [38], respectively. Additionally, the peak at 775.26 eV indicates the presence of Co-P bonding [32]. Notably, the Co 2p XPS peaks shift toward a higher binding energy compared with the NiCoP/NF sample, suggesting a higher oxidation of Co sites in NiCoP/NiO than in NiCoP/NF. As depicted in Figure 3e, the peak of the P 2p spectra located at 130.1 eV is attributed to the typical feature of metal-P bonding (M-P, Ni-P/Co-P) of metal phosphides [39], indicating a much more metallic state around the surface of NiCoP. Moreover, a new peak at higher binding energy is assigned to the bond of P-O, which may have originated from bonding with O atom in NiO or partial surficial oxidation due to exposed to air [40–42]. The above results further demonstrate that the Co and Ni atomic triggers the electron transfer from Co and Ni to P sites in the NiCoP/NiO. The charge transfer and the induced local charge redistribution, which provide the possibility of regulating the surface electronic structure of NiCoP/NiO, further verified the strong electronic interaction between NiO and NiCoP, which helps to improve the electrical conductivity and promotes the adsorption of OH[−] ions in electrolytes to participate in redox reactions [43]. As for the O 1s spectrum (Figure 3f), it was investigated to further confirm the formation of the P-O bond. Three peaks are observed in the O 1s spectrum of NiCoP/NiO, in which one at 531.0 eV is identified as M-O species (M = Co, Ni), one at 531.88 eV is attributed to oxygen defects, and another one at 533.28 eV suggests the presence of P-O bonds [32,37]. The O 1s spectrum of NiCoP/NF is similar in deconvoluted peaks to that of NiCoP/NiO. With regard to the NiO/NF, the peak at 529.0 eV was assigned to the lattice oxygen (O_{Latt}), whereas the peak at 531.1 eV was associated with absorbed oxygen (O_{Ads}) [44–46]. The results of XPS and HRTEM show that the NiCoP/NiO heterogeneous interface with a strong interface interaction is successfully formed between NiCoP and NiO, which is expected to enhance the electron transfer during the charging and discharging process, and is conducive to improving the rate performance.

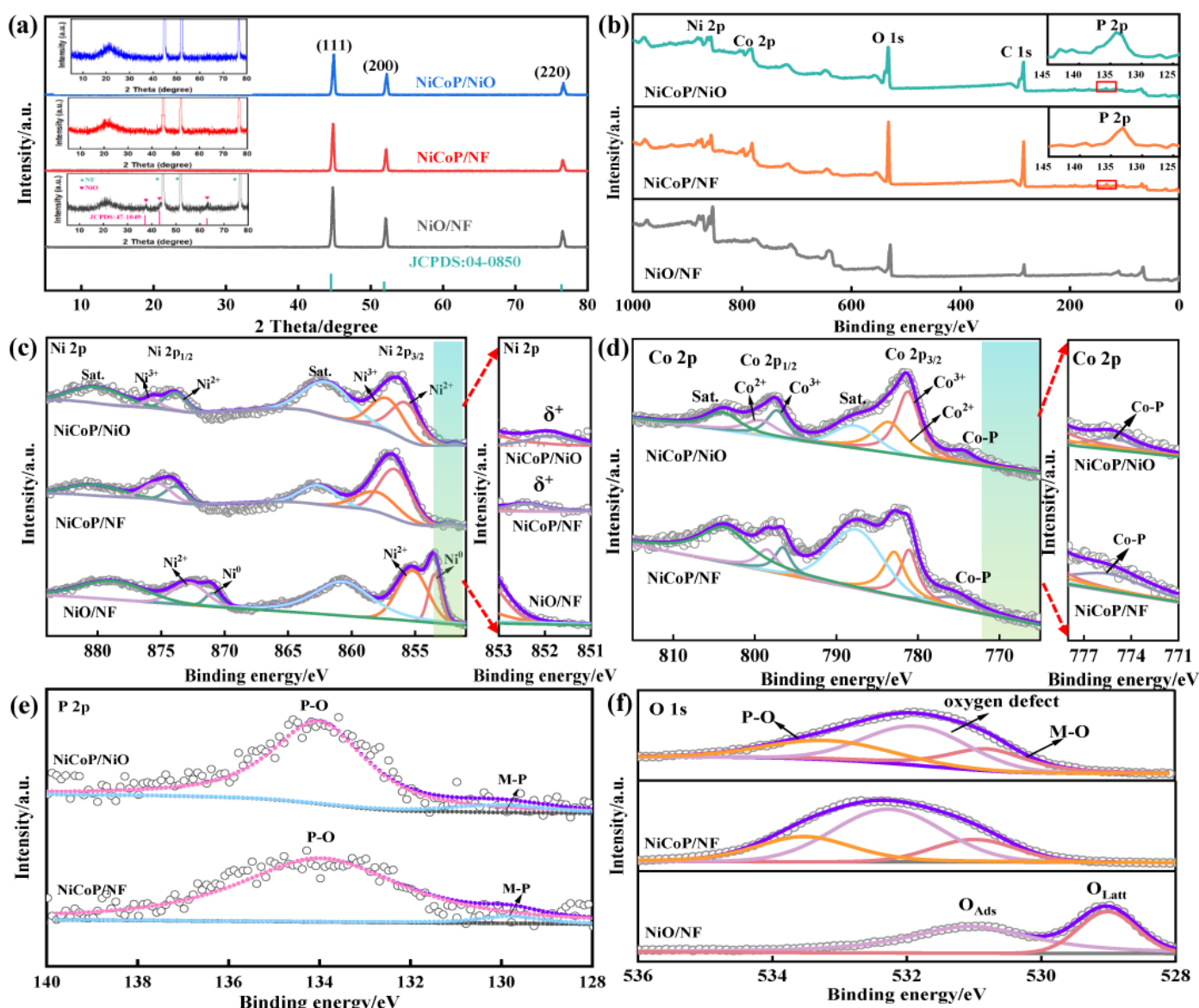
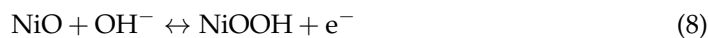
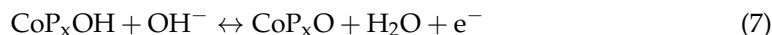


Figure 3. (a) XRD patterns of NiO/NF, NiCoP/NF and NiCoP/NiO on nickel foam. XPS spectrum of NiO/NF, NiCoP/NF and NiCoP/NiO: (b) survey; (c) Ni 2p; (d) Co 2p; (e) P 2p; and (f) O 1s, respectively.

3.2. Electrochemical Analysis

Electrochemical behaviors of the electrodes are evaluated in a three-electrode configuration. As displayed in Figure 4a, a pair of redox peaks appeared in the CV curves of the three materials measured at 10 mV s^{-1} , representing the pseudo-capacitive behavior of each electrode. Notably, the NiO/NF electrode displays one broad oxidation peak and two well-defined reduction peaks, which is most likely due to pseudocapacitive NiO and NiOOH. The latter may be generated by the electrochemical oxidation of NF in alkaline electrolyte. Compared with NiCoP/NF, the voltage difference in the redox peaks for the NiCoP/NiO electrode is 0.206 mV, which is lower than that of the NiCoP/NF electrode (0.220 mV), manifesting the enhanced electrochemical polarization and reversibility of the NiCoP/NiO electrode. Furthermore, the NiCoP/NiO electrode exhibits much larger CV curve enclosed areas, suggesting that the significantly enhanced charge storage capability due to the porous NiO nanowalls provides a larger accessible area for loading NiCoP.

Only one pair of broad redox peaks is observed because of similar redox potentials of the following reactions. The involved Faradaic redox reactions are listed as follows [39,47,48]:



All the GCD curves show distinct charge and discharge plateaus (Figure 4b), further demonstrating a pseudo-capacitive storage mechanism, which is in good agreement with the redox peaks from the CV profiles. The symmetrical charge–discharge curve also verifies the highly reversible pseudocapacitance reactions at the interface of the electrode by adsorbing the OH^- ions. Among them, the NiCoP/NiO has the longest discharging time, corresponding to the highest specific capacitance of 1860 mF cm^{-2} , compared to NiCoP/NF (1357 mF cm^{-2}) and NiO/NF (233 mF cm^{-2}) electrodes. It indicates that the existence of porous NiO nanowalls can significantly boost the areal capacitance. Figure 4c illustrates the CV curves of NiCoP/NiO electrode at $2\text{--}50 \text{ mV s}^{-1}$. It is obvious that the positions of the redox peaks (peak 1 and peak 2) shift toward higher and lower potential directions gradually as the scan rate increases. The main reason for this phenomenon is that the polarization effect resulted from the electrolyte diffusion in the active materials [49]. GCD plots of the NiCoP/NiO electrode at current densities of $5\text{--}30 \text{ mA cm}^{-2}$ exhibit almost symmetric profiles (Figure 4d), signifying highly reversible redox reactions and the excellent Coulombic efficiency during the charging–discharging process. Due to high-efficiency utilization of electroactive materials, the NiCoP/NiO electrode afforded the highest areal specific capacitance, which is much higher than NiCoP/NF and NiO/NF electrodes at the same current density (Figure 4e). CV and GCD profiles of NiO/NF and NiCoP/NF electrodes are displayed in Figure S4. Noticeably, the capacitance retention of the NiCoP/NiO, NiCoP/NF and NiO/NF electrodes is 78.5%, 55.3% and 37.3% when the current density is increased to 30 mA cm^{-2} , indicating the high capacitance and excellent rate capability of the NiCoP/NiO electrode. This can be attributed to the synergistic effect from the rapid electron transport of highly conductive porous NiO nanosheets anchored on the NF matrix and continuous network-structure NiCoP nanosheets with more exposed active sites, which improve the reaction kinetics due to effective ions and electron transport channel for rapid redox reactions [50]. Furthermore, EIS measurements were performed to gain an insight into the ion/electron diffusion kinetics of NiO/NF, NiCoP/NF and NiCoP/NiO electrodes within the range of $0.01 \text{ Hz}\text{--}100 \text{ kHz}$ (Figure 4f). Equivalent series resistance (R_s) includes the electrolyte resistance, electrode internal resistance, and contact resistance at electrode interfaces, and is represented by the intercept with respect to the x -axis [51]. All the electrodes show low R_s , which mainly attributes to the intense attachment of active materials on the current collector. The NiCoP/NiO electrode displays the smallest charge transfer resistance (R_{ct}) of 0.03Ω , suggesting NiO significantly reduces the R_{ct} of NiCoP, and the resulting hybrid structure has the fast charge transfer process. The slope of the line at low frequencies related to ion diffusion (Z_w) in the NiCoP/NiO electrode is largest, indicating the accelerated ion diffusion in the electrode via the hierarchical porous structures. The above results demonstrate that the designed NiCoP/NiO electrode exhibits enhanced electrical conductivity and fast ion accessibility, beneficial for high-efficiency charge transfer kinetics, and thus boosting the redox reaction kinetics. In addition, cycling stability is an importance index for assessing the properties of electrode materials. The electrochemical stability of NiCoP/NiO electrodes and its contrast samples were performed by repeated GCD measurements at 30 mA cm^{-2} . The NiCoP/NF electrode shows unsatisfactory stability with approximately 48% remaining after 10,000 cycles (Figure 4g). Encouragingly, the NiCoP/NiO electrode delivers a capacitance retention of 89% with an ultralow capacitance decay rate of 0.0011% per cycle, demonstrating the importance of in situ grown porous NiO nanowalls, which provide enriched anchoring

sites for confining the NiCoP and effectively improving the stability of NiCoP. Additionally, the GCD curves of the NiCoP/NiO electrode in the initial and last 10 cycles are almost symmetric and the Coulombic efficiency reached nearly 100% (Figure 4h), indicating its excellent charge–discharge reversibility.

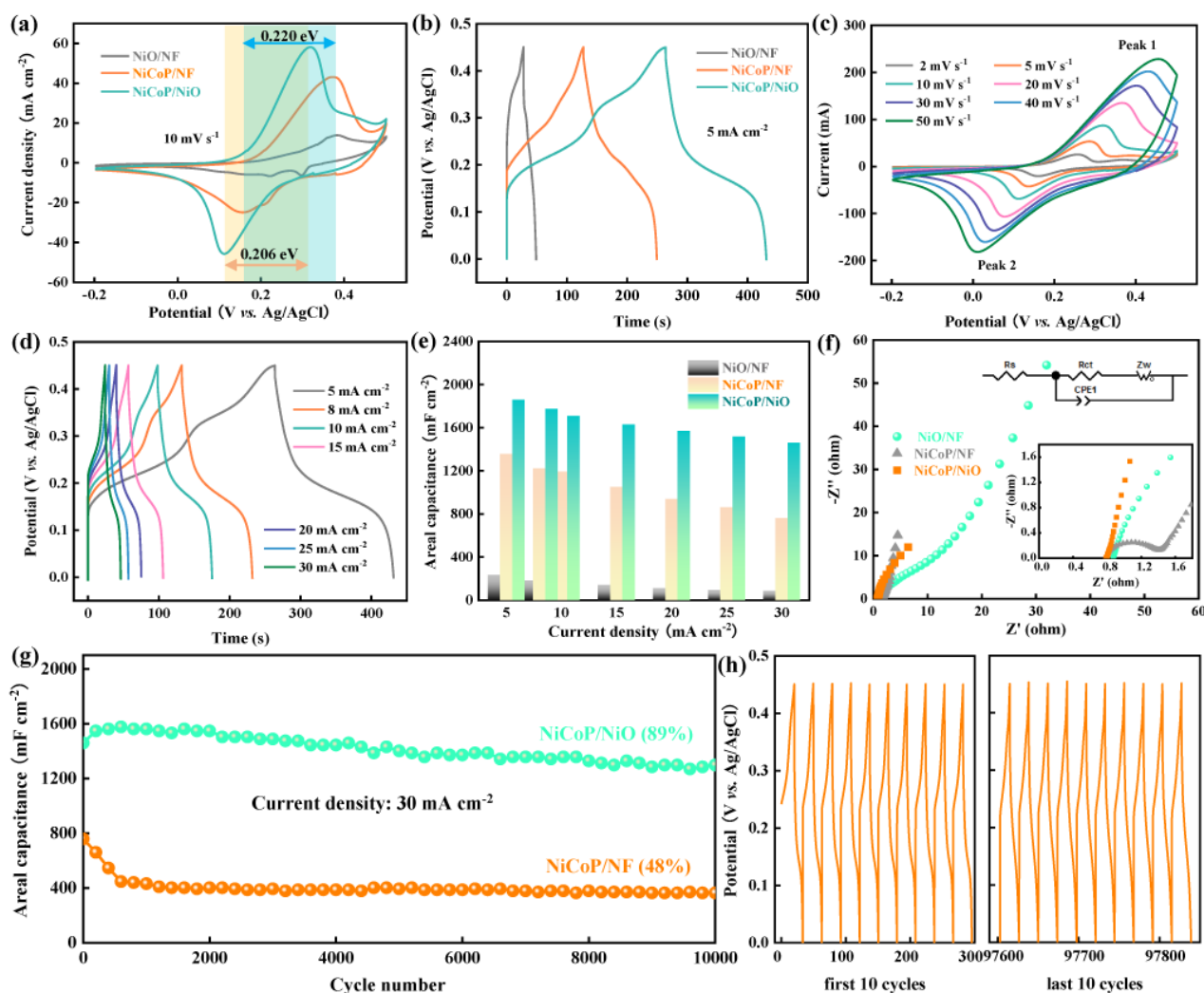


Figure 4. (a,b) CV and GCD curves of the NiO/NF, NiCoP/NF and NiCoP/NiO electrodes. (c,d) CV and GCD curves of the NiCoP/NiO electrode at various scan rates and current densities. (e) Areal capacitance retention. (f) Nyquist plots with inset showing the amplification in high frequency region. (g) Cycle performances and (h) GCD curves of the first and last 10 cycles for NiO/NiCoP electrode.

CV curves were analyzed in detail to understand the charge storage mechanism and kinetic behaviors. Generally, the capacitance contribution is composed of the diffusion-controlled and capacitive-controlled processes. Kinetic reversibility of electrode materials can be elucidated by the linear relationship between peak current (i) and scan rate (v) in CV curves, which is given according to a power–law relationship [52]:

$$i = av^b \quad (9)$$

In which a and b are undetermined parameters. Generally, there are two well-defined extremes for the b -value. The electrode kinetics conform to the diffusion-controlled mechanism ($k_2 v^{1/2}$) when $b = 0.5$, while $b = 1.0$ indicates the system is mainly controlled by a capacitive process ($k_1 v$) [28].

For the NiCoP/NiO electrode, both the b -values are 0.67, calculated from the slope of $\log(i)$ versus $\log(v)$ for peak 1 and peak 2 (Figure 5a). The estimated b values of the NiCoP/NF electrode for peak 1 and peak 2 are 0.70 and 0.68, respectively (Figure 5b). This indicates the charge storage mechanism for two electrodes is governed together with diffusion- and capacitive-processes. It can be expressed as the following equation [53]:

$$i(v) = k_1 v + k_2 v^{1/2} \text{ or } i(v)/v^{1/2} = k_1 v^{1/2} + k_2 \quad (10)$$

where $i(v)$ represents the peak current; v is the sweep rate; constants k_1 and k_2 are achieved from the slope and intercept. The contribution ratio of the surface-controlled capacitive for the NiCoP/NiO electrode at 10 mV s^{-1} is calculated to be 47.0% (Figure 5c), which is higher than that of the NiCoP/NF electrode (20.3%) (Figure 5d). Moreover, the separation of the surface- and diffusion-controlled currents at different scan rates for NiCoP/NiO and NiCoP/NF electrodes are shown in Figures S5 and S6. As the scan rate increases from 2 to 50 mV s^{-1} , both of the NiCoP/NiO and NiCoP/NF electrodes show the surface-controlled capacity proportion increases whereas the diffusion-controlled capacitive contribution decreases (Figure 5e,f), which can be related to the restricted diffusion of electrolyte ions within the electrode material at high sweep speeds. Specifically, the diffusion-controlled contribution gradually decreases at higher sweep rates due to the limited diffusion time [48], so the surface-controlled process dominates total capacitance. This effectively validates the significant rate performance of the NiCoP/NiO electrode, thanks to numerous electroactive sites and shortened ion diffusion paths. Compared with the NiCoP/NF, the NiCoP/NiO electrode has a higher surface-controlled capacitive, which may result from the advantages of its heterostructure with abundant electrochemical active sites and high porosity, as well as shortened ion diffusion pathways.

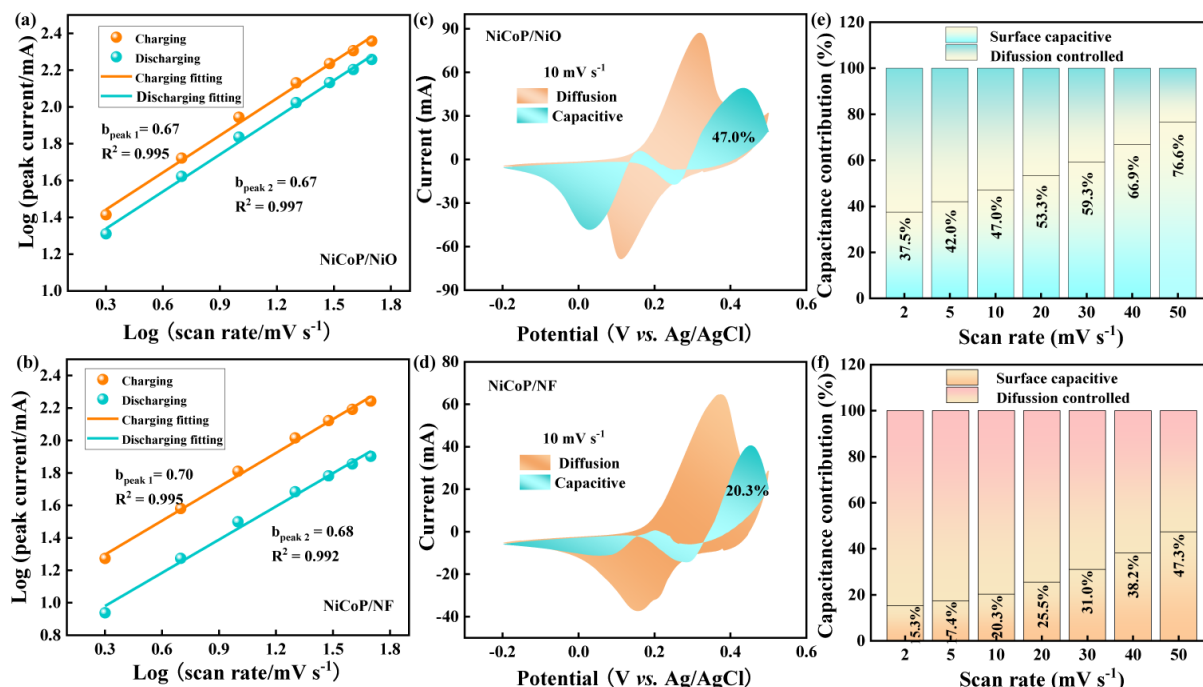


Figure 5. Plots of $\log(i_p)$ vs. $\log(v)$ for NiCoP/NiO and NiCoP/NF electrodes (a,b). Capacitive contribution of NiCoP/NiO and NiCoP/NF electrodes at 10 mV s^{-1} (c,d). Capacitive capacity contribution ratios of NiCoP/NiO and NiCoP/NF electrodes at different scan rates (e,f).

Considering the excellent electrochemical performances of the NiCoP/NiO electrode, the asymmetric supercapacitor NiCoP/NiO//PAC was assembled to investigate its practicability (Figure 6a). The device consists of the NiCoP/NiO positive electrode operated at $-0.2\text{--}0.5 \text{ V}$ and PAC negative electrode occupied from -1.0 to 0 V (Figure 6b). The detailed

electrochemical behavior of the PAC electrode is shown in Figure S7, which demonstrates excellent electric double-layer capacitance characteristics. It can be seen from Figure 6c that the working voltage of the hybrid supercapacitor reaches 1.6 V, and the shape of the CV curve does not change significantly at high scanning rates, demonstrating its typical pseudo-capacitive properties [54]. The GCD plots display nearly symmetrical features (Figure 6d), implying their good electrochemical reversibility and high Coulombic efficiencies at various current densities. It is worth mentioning that low IR drops of the constructed ASC device were observed, demonstrating low internal resistance as well as outstanding rate performance. The ASC delivers the enhanced areal specific capacitance of 489, 465, 433, 381, 349 and 328 mF cm⁻² at 2~40 mA cm⁻². It retains the capacitance retention of 88.5% at 10 mA cm⁻² and 67.1% at a current density of up to 40 mA cm⁻² (Figure 6e), suggesting its outstanding rate capability. Areal energy density (E_a) and areal power density (P_a) are significant criteria to estimate the energy storage capacity and discharge speed of supercapacitors in practical application. Ragone plots of the NiCoP/NiO//PAC and some other hybrid devices previously reported in the literature are shown in Figure 6f. Note that the maximum energy density achieved by the NiCoP/NiO//PAC ASC was 173.7 μWh cm⁻² at 1.6 mW cm⁻². Moreover, the NiCoP/NiO//PAC delivers the high power density of 32 mW cm⁻² while it still can provide high energy density of 116.4 μWh cm⁻², indicating the NiCoP/NiO//PAC ASC has a promising power capability, which is competitive with reported works (Table S1), such as NF/NiO/NiCo₂S₄//AC/NF (25.4 μWh cm⁻² at 0.782 mW cm⁻²) [14], NiCo₂S₄@NiCoP/NF//AC (0.135 mWh cm⁻² at 0.755 mW cm⁻²) [9], NiCo₂S₄@CNT//Ti₃C₂T_x@CCT (0.18 mWh cm⁻² at 2 mW cm⁻²) [55], NiCo₂O₄ NG@CF//porous carbon@CF (9.46 μWh cm⁻² at 608.4 μW cm⁻²) [56], Co_{0.8}Ni_{0.2}Se₂//AC (0.071 mWh cm⁻² at 0.75 mW cm⁻²) [57], and Ni_aCo_bS@NF//AC (1.25 μWh cm⁻² at 6 mW cm⁻²) [58]. In addition, Figure 6g shows the durability of the supercapacitor device is conducted at 40 mA cm⁻². Remarkably, it retains about 74% initial capacitance with a Coulombic efficiency of almost 100% over 5000 cycles, exhibiting a considerable cycling lifespan and further verifying its satisfied actual application. This is mainly due to the strong interaction at the interfaces of NiO/nickel foam and NiCoP/NiO, which can avoid the active material shedding from the substrate surface during the continuous charging and discharging process and ensures the structural stability [59]. EIS measurement of the NiCoP/NiO//PAC ASC was conducted to observe the change of resistance before and after cycling. Both the R_s and R_{ct} increase slightly in Nyquist plots after 5000 cycles (Figure 6h), which is in accordance with its stability with slight decay. Meanwhile, the ion diffusion resistance (R_w) still remains low and shows almost no change, indicating its high ionic accessibility in the progress of consecutive charging and discharging.

To investigate the practicability of the device, the device was used to power different electronic devices. Surprisingly, when connecting the two ASC devices in series, the working voltage output rose up to 3.2 V (Figure 7a,b), which was applied to power a red light-emitting diode (LED) with a driven voltage of 2.2~2.4 V (Figure 7e), demonstrating the practical feasibility of the device. Furthermore, a digital timer could also be illuminated by linking two devices in series as a power source for over 25 min (Figure 7e). For comparison, we also assembled an NiCoP/NF//PAC ASC device. When the two devices are connected in series, the devices can reach the same operating voltage, but there is a more obvious polarization phenomenon and a smaller discharge capacitance than the NiCoP/NiO//PAC devices (Figure 7c,d). Two devices in series can light the above LED for about 10 min (Figure 7f). However, it did not light up the calculator. The results show that the NiCoP/NiO//PAC device exhibits a general energy storage effect. These provide actual viable demonstrations that the as-fabricated hybrid ASC devices are highly promising for use in the field of energy applications in the future.

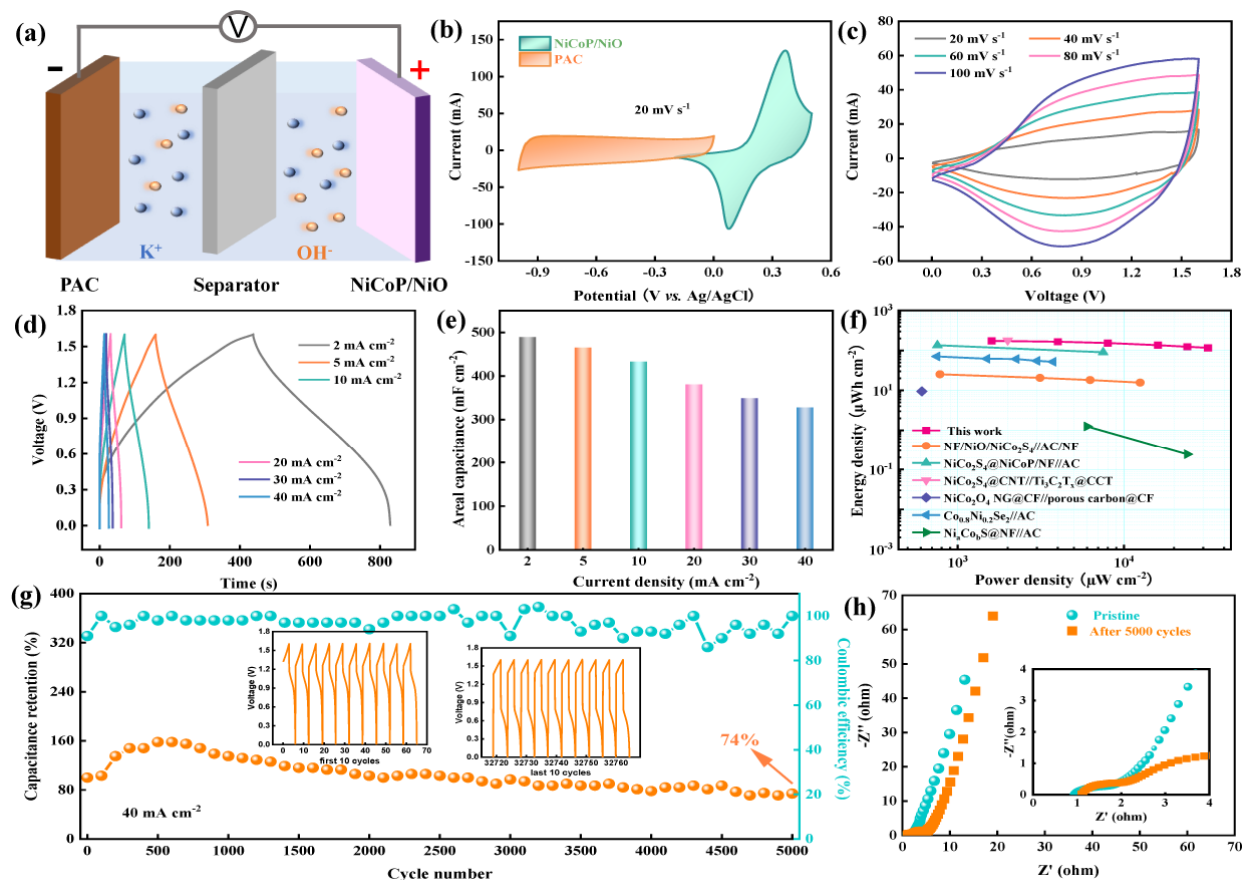


Figure 6. (a) Schematic diagram of supercapacitor; (b) CV curves of NiCoP/NiO and PAC electrodes at 20 mV s^{-1} . Electrochemical performance of the NiCoP/NiO//PAC ASC: (c) CV plots; (d) GCD curves; (e) areal capacitance at various current densities; (f) Ragone plot; (g) cycling stability; and (h) Nyquist plot.

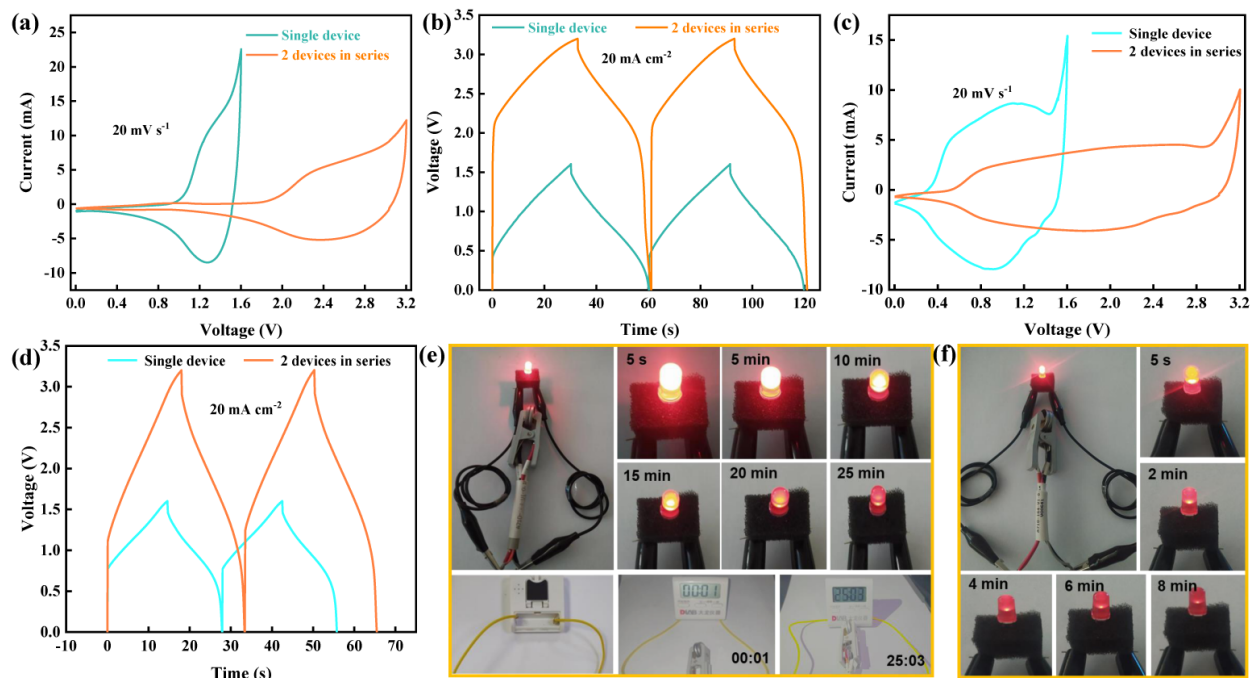


Figure 7. CV and GCD curves of the single NiCoP/NiO//PAC device and two ones connected in series (a,b). Photos of two NiCoP/NiO//PAC devices connected in series light up LED and digital timer (e).

CV and GCD curves of the single NiCoP/NF//PAC device and two ones connected in series (c,d). Photos of two devices of NiCoP/NF//PAC connected in series light up LED (f).

4. Conclusions

In this work, we proposed a facile approach to synthesize the NiCoP/NiO nanocomposites over nickel foam by in situ oxidation–heat treatment followed by electrodeposition. The special hierarchical porous structure provides the NiCoP/NiO with strong electrochemically synergistic interactions, benefiting for improving electronic transport, shorting ions transport pathways, and increased electrode/electrolyte interfaces. The optimized NiCoP/NiO electrode possesses a remarkable electrochemical performance with high areal specific capacitance, high-rate performance and long-term cycling life. In addition, the as-assembled ASC delivers high energy density of $173.7 \mu\text{Wh cm}^{-2}$ at 1.6 mW cm^{-2} and satisfactory cycling stability of about 74% retention after 5000 cycles. Furthermore, two series devices can drive both an LED and digital timer to work for over 25 min, indicating its great prospect as a type of advanced electrode material for supercapacitors.

Supplementary Materials: The following supporting information can be downloaded at: <https://www.mdpi.com/article/10.3390/batteries9120584/s1>, Figure S1: SEM images of (a,b) pure nickel foam and (c,d) NiO/NF at different magnifications; Figure S2: SEM images of NiCoP/NiO nanocomposites with electrodeposition time of 15 min; Figure S3: N_2 adsorption-desorption isotherms of the NiO/NiCoP and NiCoP; Figure S4: Electrochemical performance measured in a three-electrode system in 2.0 M KOH electrolyte: CV curves and GCD curves of the (a,b) NiO/NF and (c,d) NiCoP/NF electrodes, respectively; Figure S5: Separation of the surface and diffusion-controlled currents at different scan rates for the NiCoP/NiO electrode; Figure S6: Separation of the surface and diffusion-controlled currents at different scan rates for the NiCoP/NF electrode; Figure S7: (a) CV curves, (b) GCD curves, and (c) areal specific capacitance of the PAC electrode; Table S1: Comparative electrochemical performance of nickel-cobalt based nanocomposite materials reported by the literature.

Author Contributions: G.Z.: Conceptualization, supervision, project administration, writing—review and editing, funding acquisition; J.L.: material fabrication and characterization, visualization, writing—original draft; H.S.: formal analysis; Z.M.: construction drawing; Y.X.: formal analysis, methodology; Z.Y.: visualization, methodology; J.Z.: formal analysis, validation; J.W.: project administration; S.L.: conceptualization; X.L.: conceptualization, funding acquisition, supervision, writing—review and editing. All authors have read and agreed to the published version of the manuscript.

Funding: This work was supported by the National Natural Science Foundation of China (22279101); the Natural Science Basic Research Plan in Shaanxi Province of China (2022JM-090); the China Postdoctoral Science Foundation (2021M693885).

Data Availability Statement: The data presented in this study are available in article.

Conflicts of Interest: The authors declare no conflict of interest. The funders had no role in the design of the study; in the collection, analyses, or interpretation of data; in the writing of the manuscript; or in the decision to publish the results.

References

- Chu, S.; Majumdar, A. Opportunities and challenges for a sustainable energy future. *Nature* **2012**, *488*, 294–303. [[CrossRef](#)] [[PubMed](#)]
- Chang, Z.; Yang, Y.; Li, M.; Wang, X.; Wu, Y. Green energy storage chemistries based on neutral aqueous electrolytes. *J. Mater. Chem. A* **2014**, *2*, 10739–10755. [[CrossRef](#)]
- Zakeri, B.; Syri, S. Electrical energy storage systems: A comparative life cycle cost analysis. *Renew. Sustain. Energy Rev.* **2015**, *42*, 569–596. [[CrossRef](#)]
- Hao, Z.; He, X.; Li, H.; Trefilov, D.; Song, Y.; Li, Y.; Fu, X.; Cui, Y.; Tang, S.; Ge, H.; et al. Vertically aligned and ordered arrays of 2D MCo_2S_4 @metal with ultrafast ion/electron transport for thickness-independent pseudocapacitive energy Storage. *ACS Nano* **2020**, *14*, 12719–12731. [[CrossRef](#)] [[PubMed](#)]
- Wang, Y.; Song, Y.; Xia, Y. Electrochemical capacitors: Mechanism, materials, systems, characterization and applications. *Chem. Soc. Rev.* **2016**, *45*, 5925–5950. [[CrossRef](#)]

6. Wang, G.; Zhang, L.; Zhang, J. A review of electrode materials for electrochemical supercapacitors. *Chem. Soc. Rev.* **2012**, *41*, 797–828. [[CrossRef](#)]
7. Raghavendra, K.V.G.; Vinoth, R.; Zeb, K.; Muralee Gopi, C.V.V.; Sambasivam, S.; Kummara, M.R.; Obaidat, I.M.; Kim, H.J. An intuitive review of supercapacitors with recent progress and novel device applications. *J. Energy Storage* **2020**, *31*, 101652. [[CrossRef](#)]
8. Cheng, X.; Zhang, J.; Ren, J.; Liu, N.; Chen, P.; Zhang, Y.; Deng, J.; Wang, Y.; Peng, H. Design of a hierarchical ternary hybrid for a fiber-shaped asymmetric supercapacitor with high volumetric energy density. *J. Phys. Chem. C* **2016**, *120*, 9685–9691. [[CrossRef](#)]
9. Chang, X.; Li, W.; Liu, Y.; He, M.; Zheng, X.; Bai, J.; Ren, Z. Hierarchical NiCo₂S₄@NiCoP core-shell nanocolumn arrays on nickel foam as a binder-free supercapacitor electrode with enhanced electrochemical performance. *J. Colloid Interface Sci.* **2019**, *538*, 34–44. [[CrossRef](#)]
10. Zhang, K.; Cen, Z.; Yang, F.; Xu, K. Rational construction of NiCo₂O₄@Fe₂O₃ core-shell nanowire arrays for high-performance supercapacitors. *Prog. Nat. Sci.* **2021**, *31*, 19–24. [[CrossRef](#)]
11. Wang, Z.; Wang, H.; Ji, S.; Wang, X.; Zhou, P.; Huo, S.; Linkov, V.; Wang, R. Hollow-structured NiCoP nanorods as high-performance electrodes for asymmetric supercapacitors. *Mater. Des.* **2020**, *193*, 108807. [[CrossRef](#)]
12. Nguyen, T.; Boudard, M.; Carmezim, M.J.; Montemor, M.F. Layered Ni(OH)₂-Co(OH)₂ films prepared by electrodeposition as charge storage electrodes for hybrid supercapacitors. *Sci. Rep.* **2017**, *7*, 39980. [[CrossRef](#)] [[PubMed](#)]
13. Zhang, B.; Liu, Q.; Xu, K.; Zou, R.; Wang, C. Electrochemical energy storage application of CuO/CuO@Ni-CoMoO₄·0.75H₂O nanobelt arrays grown directly on Cu foam. *Prog. Nat. Sci.* **2022**, *32*, 163–170. [[CrossRef](#)]
14. Moradlou, O.; Sharifpour, H. Interconnected NiCo₂S₄-coated NiO nanosheet arrays as electrode materials for high-performance supercapacitors. *J. Energy Storage* **2020**, *32*, 101886. [[CrossRef](#)]
15. Xu, R.; Lin, J.; Wu, J.; Huang, M.; Fan, L.; Chen, H.; He, X.; Wang, Y.; Xu, Z. Two-step hydrothermal synthesis of NiCo₂S₄/Co₉S₈ nanorods on nickel foam for high energy density asymmetric supercapacitors. *Appl. Surf. Sci.* **2018**, *434*, 861–870. [[CrossRef](#)]
16. Ren, F.; Ji, Y.; Tan, S.; Chen, F. Sponge-like NiCo₂S₄ nanosheets supported on nickel foam as high-performance electrode materials for asymmetric supercapacitors. *Inorg. Chem. Front.* **2020**, *8*, 72–78. [[CrossRef](#)]
17. Xie, S.; Gou, J. Facile synthesis of Ni₂P/Ni₁₂P₅ composite as long-life electrode material for hybrid supercapacitor. *J. Alloys Compd.* **2017**, *713*, 10–17. [[CrossRef](#)]
18. Zhang, X.; Su, D.; Wu, A.; Yan, H.; Wang, X.; Wang, D.; Wang, L.; Tian, C.; Sun, L.; Fu, H. Porous NiCoP nanowalls as promising electrode with high-area and mass capacitance for supercapacitors. *Sci. China Mater.* **2019**, *62*, 1115–1126. [[CrossRef](#)]
19. Wang, L.; Feng, Z.; Zhang, H.; Li, D.; Xing, P. One-step electrodeposited 3D porous NiCoSe₂ nanosheet array for high-performance asymmetric supercapacitors. *Nanotechnology* **2020**, *31*, 125403. [[CrossRef](#)]
20. Ye, B.; Cao, X.; Zhao, Q.; Zhou, A.; Wang, J. Free-standing NiCoSe₂ nanostructure on Ni foam via electrodeposition as high-performance asymmetric supercapacitor electrode. *Nanotechnology* **2020**, *31*, 335706. [[CrossRef](#)]
21. Liu, Q.; Hu, R.; Qi, J.; Sui, Y.; He, Y.; Meng, Q.; Wei, F.; Ren, Y. Facile synthesis of hierarchical NiCoP nanowires@NiCoP nanosheets core-shell nanoarrays for high-performance asymmetrical supercapacitor. *J. Mater. Sci.* **2019**, *55*, 1157–1169. [[CrossRef](#)]
22. Li, X.; Elshahawy, A.M.; Guan, C.; Wang, J. Metal phosphides and phosphates-based electrodes for electrochemical supercapacitors. *Small* **2017**, *13*, 1701530. [[CrossRef](#)] [[PubMed](#)]
23. Kong, M.; Wang, Z.; Wang, W.; Ma, M.; Liu, D.; Hao, S.; Kong, R.; Du, G.; Asiri, A.M.; Yao, Y.; et al. NiCoP nanoarray: A superior pseudocapacitor electrode with high areal capacitance. *Chemistry* **2017**, *23*, 4435–4441. [[CrossRef](#)] [[PubMed](#)]
24. Zhang, N.; Li, Y.; Xu, J.; Li, J.; Wei, B.; Ding, Y.; Amorim, I.; Thomas, R.; Thalluri, S.M.; Liu, Y.; et al. High-performance flexible solid-state asymmetric supercapacitors based on bimetallic transition metal phosphide nanocrystals. *ACS Nano* **2019**, *13*, 10612–10621. [[CrossRef](#)] [[PubMed](#)]
25. Chen, H.; Chen, S.; Fan, M.; Li, C.; Chen, D.; Tian, G.; Shu, K. Bimetallic nickel cobalt selenides: A new kind of electroactive material for high-power energy storage. *J. Mater. Chem. A* **2015**, *3*, 23653–23659. [[CrossRef](#)]
26. Hu, Y.-M.; Liu, M.-C.; Hu, Y.-X.; Yang, Q.-Q.; Kong, L.-B.; Kang, L. One-pot hydrothermal synthesis of porous nickel cobalt phosphides with high conductivity for advanced energy conversion and storage. *Electrochim. Acta* **2016**, *215*, 114–125. [[CrossRef](#)]
27. Huang, J.; Xiong, Y.; Peng, Z.; Chen, L.; Wang, L.; Xu, Y.; Tan, L.; Yuan, K.; Chen, Y. A general electrodeposition strategy for fabricating ultrathin nickel cobalt phosphate nanosheets with ultrahigh capacity and rate performance. *ACS Nano* **2020**, *14*, 14201–14211. [[CrossRef](#)]
28. Wan, L.; Wang, Y.; Zhang, Y.; Du, C.; Chen, J.; Xie, M.; Tian, Z.; Zhang, W. Designing FeCoP@NiCoP heterostructured nanosheets with superior electrochemical performance for hybrid supercapacitors. *J. Power Sources* **2021**, *506*, 230096. [[CrossRef](#)]
29. Hang, X.; Xue, Y.; Zhao, J.; Yang, R.; Pang, H. In situ generation of NiCoP nanoparticles on a bimetal-organic framework for high-performance supercapacitors. *Inorg. Chem.* **2022**, *61*, 10435–10441. [[CrossRef](#)]
30. Anuratha, K.S.; Su, Y.-Z.; Huang, M.-K.; Hsieh, C.-K.; Xiao, Y.; Lin, J.-Y. High-performance hybrid supercapacitors based on electrodeposited amorphous bimetallic nickel cobalt phosphide nanosheets. *J. Alloys Compd.* **2022**, *897*, 163031. [[CrossRef](#)]
31. Zhang, X.; Wu, A.; Wang, X.; Tian, C.; An, R.; Fu, H. Porous NiCoP nanosheets as efficient and stable positive electrodes for advanced asymmetric supercapacitors. *J. Mater. Chem. A* **2018**, *6*, 17905–17914. [[CrossRef](#)]
32. Hu, X.; Fan, J.; Wang, R.; Li, M.; Sun, S.; Xu, C.; Pan, F. Vacancies and interfaces engineering of core–shell heterostuctured NiCoP/NiO as trifunctional electrocatalysts for overall water splitting and zinc-air batteries. *Green Energy Environ.* **2021**, *8*, 601–611. [[CrossRef](#)]

33. Liu, Q.; Tian, J.; Cui, W.; Jiang, P.; Cheng, N.; Asiri, A.M.; Sun, X. Carbon nanotubes decorated with CoP nanocrystals: A highly active non-noble-metal nanohybrid electrocatalyst for hydrogen evolution. *Angew. Chem. Int. Ed. Engl.* **2014**, *53*, 6710–6714. [[CrossRef](#)] [[PubMed](#)]
34. Jiang, P.; Liu, Q.; Liang, Y.; Tian, J.; Asiri, A.M.; Sun, X. A cost-effective 3D hydrogen evolution cathode with high catalytic activity: FeP nanowire array as the active phase. *Angew. Chem. Int. Ed. Engl.* **2014**, *53*, 12855–12859. [[CrossRef](#)] [[PubMed](#)]
35. Ali, A.; Ammar, M.; Mukhtar, A.; Ahmed, T.; Ali, M.; Waqas, M.; Amin, M.N.; Rasheed, A. 3D NiO nanowires@NiO nanosheets core-shell structures grown on nickel foam for high performance supercapacitor electrode. *J. Electroanal. Chem.* **2020**, *857*, 113710. [[CrossRef](#)]
36. Qu, G.; Sun, P.; Xiang, G.; Yin, J.; Wei, Q.; Wang, C.; Xu, X. Moss-like nickel-cobalt phosphide nanostructures for highly flexible all-solid-state hybrid supercapacitors with excellent electrochemical performances. *Appl. Mater. Today* **2020**, *20*, 100713. [[CrossRef](#)]
37. Liu, H.; Ma, X.; Hu, H.; Pan, Y.; Zhao, W.; Liu, J.; Zhao, X.; Wang, J.; Yang, Z.; Zhao, Q.; et al. Robust NiCoP/CoP heterostructures for highly efficient hydrogen evolution electrocatalysis in alkaline solution. *ACS Appl. Mater. Interfaces* **2019**, *11*, 15528–15536. [[CrossRef](#)]
38. Yang, X.; Lu, A.-Y.; Zhu, Y.; Hedhili, M.N.; Min, S.; Huang, K.-W.; Han, Y.; Li, L.-J. CoP nanosheet assembly grown on carbon cloth: A highly efficient electrocatalyst for hydrogen generation. *Nano Energy* **2015**, *15*, 634–641. [[CrossRef](#)]
39. Li, P.; Han, Y.; Yan, F.; Yan, L.; Huang, H.; Zhou, W. Engineering NiCoP arrays by cross-linked nanowires and nanosheets as advanced materials for hybrid supercapacitors. *J. Energy Storage* **2021**, *38*, 102503. [[CrossRef](#)]
40. Zhu, Y.; An, S.; Sun, X.; Lan, D.; Cui, J.; Zhang, Y.; He, W. Core-branched NiCo₂S₄@CoNi-LDH heterostructure as advanced electrode with superior energy storage performance. *Chem. Eng. J.* **2020**, *383*, 123206. [[CrossRef](#)]
41. Wang, M.; Zhong, J.; Zhu, Z.; Gao, A.; Yi, F.; Ling, J.; Hao, J.; Shu, D. Hollow NiCoP nanocubes derived from a prussian blue analogue self-template for high-performance supercapacitors. *J. Alloys Compd.* **2022**, *893*, 162344. [[CrossRef](#)]
42. Liang, H.; Xia, C.; Jiang, Q.; Gandi, A.N.; Schwingenschlögl, U.; Alshareef, H.N. Low temperature synthesis of ternary metal phosphides using plasma for asymmetric supercapacitors. *Nano Energy* **2017**, *35*, 331–340. [[CrossRef](#)]
43. Ni, S.; Qu, H.; Xu, Z.; Zhu, X.; Xing, H.; Wang, L.; Yu, J.; Liu, H.; Chen, C.; Yang, L. Interfacial engineering of the NiSe₂/FeSe₂ p-p heterojunction for promoting oxygen evolution reaction and electrocatalytic urea oxidation. *Appl. Catal. B* **2021**, *299*, 120638. [[CrossRef](#)]
44. Kim, S.-Y.; Gopi, C.V.V.M.; Reddy, A.E.; Kim, H.-J. Facile synthesis of a NiO/NiS hybrid and its use as an efficient electrode material for supercapacitor applications. *New J. Chem.* **2018**, *42*, 5309–5313. [[CrossRef](#)]
45. Wu, S.; Hui, K.S.; Hui, K.N.; Kim, K.H. Ultrathin porous NiO nanoflake arrays on nickel foam as an advanced electrode for high performance asymmetric supercapacitors. *J. Mater. Chem. A* **2016**, *4*, 9113–9123. [[CrossRef](#)]
46. Liu, X.; Liu, J.; Sun, X. NiCo₂O₄@NiO hybrid arrays with improved electrochemical performance for pseudocapacitors. *J. Mater. Chem. A* **2015**, *3*, 13900–13905. [[CrossRef](#)]
47. Jin, Y.; Zhao, C.; Jiang, Q.; Ji, C. Mesoporous NiCoP microflowers as a superior electrode material for supercapacitors. *Appl. Surf. Sci.* **2018**, *450*, 170–179. [[CrossRef](#)]
48. Wang, X.; Jing, C.; Zhang, W.; Wang, X.; Liu, X.; Dong, B.; Zhang, Y. One-step phosphorization synthesis of CoP@NiCoP nanowire/nanosheet composites hybrid arrays on Ni foam for high-performance supercapacitors. *Appl. Surf. Sci.* **2020**, *532*, 147437. [[CrossRef](#)]
49. Wang, H.; Zhu, Y.; Zong, Q.; Wang, Q.; Yang, H.; Zhang, Q. Hierarchical NiCoP/Co(OH)₂ nanoarrays for high-performance asymmetric hybrid supercapacitors. *Electrochim. Acta* **2019**, *321*, 134746. [[CrossRef](#)]
50. Shanmugam Anuratha, K.; Su, Y.Z.; Wang, P.J.; Hasin, P.; Wu, J.; Hsieh, C.K.; Chang, J.K.; Lin, J.Y. Free-standing 3D core-shell architecture of Ni₃S₂@NiCoP as an efficient cathode material for hybrid supercapacitors. *J. Colloid Interface Sci.* **2022**, *625*, 565–575. [[CrossRef](#)] [[PubMed](#)]
51. Yang, Y.; Li, L.; Ruan, G.; Fei, H.; Xiang, C.; Fan, X.; Tour, J.M. Hydrothermally formed three-dimensional nanoporous Ni(OH)₂ thin-film supercapacitors. *ACS Nano* **2014**, *8*, 9622–9628. [[CrossRef](#)]
52. Augustyn, V.; Come, J.; Lowe, M.A.; Kim, J.W.; Taberna, P.L.; Tolbert, S.H.; Abruna, H.D.; Simon, P.; Dunn, B. High-rate electrochemical energy storage through Li⁺ intercalation pseudocapacitance. *Nat. Mater.* **2013**, *12*, 518–522. [[CrossRef](#)] [[PubMed](#)]
53. Liang, M.; Zhao, M.; Wang, H.; Shen, J.; Song, X. Enhanced cycling stability of hierarchical NiCo₂S₄@Ni(OH)₂@PPy core-shell nanotube arrays for aqueous asymmetric supercapacitors. *J. Mater. Chem. A* **2018**, *6*, 2482–2493. [[CrossRef](#)]
54. Chen, F.; Ji, S.; Liu, Q.; Wang, H.; Liu, H.; Brett, D.J.L.; Wang, G.; Wang, R. Rational design of hierarchically core-shell structured Ni₃S₂@NiMoO₄ nanowires for electrochemical energy storage. *Small* **2018**, *14*, e1800791. [[CrossRef](#)] [[PubMed](#)]
55. Yu, J.; Zhou, J.; Yao, P.; Huang, J.; Sun, W.; Zhu, C.; Xu, J. A stretchable high performance all-in-one fiber supercapacitor. *J. Power Sources* **2019**, *440*, 227150. [[CrossRef](#)]
56. Senthilkumar, S.T.; Fu, N.; Liu, Y.; Wang, Y.; Zhou, L.; Huang, H. Flexible fiber hybrid supercapacitor with NiCo₂O₄ nanograss@carbon fiber and bio-waste derived high surface area porous carbon. *Electrochim. Acta* **2016**, *211*, 411–419. [[CrossRef](#)]
57. Sheng, P.; Ye, R.; Wu, D.; Zhang, L.; An, X.; Tao, S.; Qian, B.; Chu, P.K. Morphological modulation of cobalt selenide on carbon cloth by Ni doping for high-performance electrodes in supercapacitors. *Colloids Surf. A Physicochem. Eng. Asp* **2021**, *624*, 126818. [[CrossRef](#)]

58. Chou, S.-H.; Lin, L.-Y.; Chiu, Y.-H. Pulse reverse electrodeposited nickel cobalt sulfide nanosheets on Ni foam as battery-type electrode for battery supercapacitor hybrids. *J. Energy Storage* **2019**, *25*, 100903. [[CrossRef](#)]
59. Chen, Q.; Cai, D.; Zhan, H. Interconnected Ni-Co sulfide nanosheet arrays grown on nickel foam as binder-free electrodes for supercapacitors with high areal capacitance. *J. Alloys Compd.* **2017**, *721*, 205–212. [[CrossRef](#)]

Disclaimer/Publisher's Note: The statements, opinions and data contained in all publications are solely those of the individual author(s) and contributor(s) and not of MDPI and/or the editor(s). MDPI and/or the editor(s) disclaim responsibility for any injury to people or property resulting from any ideas, methods, instructions or products referred to in the content.